






PAPER

[View Article Online](#)
[View Journal](#) | [View Issue](#)Cite this: *Catal. Sci. Technol.*, 2019,
9, 3203**Au/Co promoted CeO₂ catalysts for formaldehyde total oxidation at ambient temperature: role of oxygen vacancies†**Guillaume Rochard, ^a Jean-Marc Giraudon, ^a Leonarda Francesca Liotta, ^{*b}
Valeria La Parola ^b and Jean-François Lamonier ^{*a}

Au catalysts with loadings of 1.5 and 3 wt% were dispersed over CeO₂ and Co (9; 12 mol%) promoted CeO₂, using the deposition-precipitation method, followed by calcination at 350 °C. The fresh supported Au catalysts were characterized using several techniques in order to investigate their morphological, structural and redox properties before being tested for formaldehyde (HCHO) total oxidation. All of the supported Au catalysts exhibited HCHO oxidation into CO₂ at 25 °C and demonstrated a great stability for the time on stream (40 h). The 3 wt% Au catalysts demonstrated a higher HCHO conversion than their low-gold counterparts (1.5 wt% Au), a remarkable improvement in the HCHO conversion was observed using Co-promoted ceria (9 mol%). Based on the HCHO amount (in μmol) converted into CO₂ per gram of gold per second after 40 h on stream, the 1.5Au/CeCo catalyst demonstrated the best activity (~3.9) as compared to the other catalysts (≤2.0). X-ray photoelectron spectroscopy (XPS) characterization of the fresh catalysts indicated that the Au species were mainly in a slightly ionic δ⁺ valence state, but did not exclude the possibility of metallic gold. Furthermore, no marked changes were found in gold dispersion upon adding cobalt. Promotion of the HCHO oxidation over gold supported on Co-promoted ceria catalysts can be related to the higher concentration of oxygen vacancies and an improvement in the redox properties, which can contribute to the better activation of O₂ and an enhancement of the oxygen mobility.

Received 5th March 2019,
Accepted 9th May 2019

DOI: 10.1039/c9cy00436j

rsc.li/catalysis**Introduction**

Formaldehyde (HCHO) is a dangerous volatile organic compound (VOC), mostly used in the wood industry as a glue component. Degradation of this glue with time allows the release of HCHO into the indoor environment. It is well known that prolonged exposure to HCHO contributes to important health issues (such as a burning sensation, breathing problems, and certain cancers).¹ This pollutant can be removed from air using several methods such as adsorption and photocatalysis. However, total oxidation by heterogeneous catalysis into harmless species (CO₂ and H₂O) is the most promising alternative.² So far, supported noble metals catalysts such as Pt, Pd and Au have been successfully used for low/room temperature catalytic oxidation of formaldehyde.^{3–6} The performance of supported metal catalysts relies on many factors, in-

cluding the metal particle size, dispersion and metal-support interactions, and differentiation of these effects is challenging in order to gain an insight into the operating mode of the catalyst. As a catalyst, gold was considered to be inert until work by Haruta *et al.*⁷ showed highly dispersed gold nanoparticles (NPs) to be very active in CO oxidation. It is commonly reported that dispersion has a significant importance for gold activity in VOC removal.⁸ However, the dispersion of gold NPs is mostly related to the mode of preparation,^{9–12} gold loading^{13–15} and calcination temperature.^{14–18} Among the different materials already used for gold deposition, such as hydroxyapatite, fluoroapatite, SiO₂, HZSM-5, Al₂O₃, FeO_x, TiO₂, and ZrO₂,^{8,11,14,16,19} CeO₂ appears to be an attractive material owing to its low-temperature redox activity, unusual oxygen storage capacity and the possibility of interacting strongly with gold.²⁰ It is well known that the electronic and redox properties of ceria are dominated by the presence of oxygen vacancies,²¹ which are thought to play a major role in catalysis.²² Sayle *et al.*²³ highlighted the correlation between the low formation energies of surface oxygen vacancies (facilitated on the (110) and (310) planes) and the CO oxidation reaction. Thus, the authors predicted that any process which preferentially exposed the (110) and (310) surfaces would enhance the activity for CO oxidation. In addition, Liu *et al.*²⁴ revealed an

^a Univ. Lille, CNRS, Centrale Lille, ENSCL, Univ. Artois, UMR 8181 – UCCS – Unité de Catalyse et Chimie du Solide, F-59000 Lille, France.E-mail: jean-francois.lamonier@univ-lille.fr^b Istituto per lo Studio dei Materiali Nanostrutturati ISMN-CNR, Via Ugo La Malfa 153, 90146 Palermo, Italy. E-mail: leonardafrancesca.liotta@cnr.it

† Electronic supplementary information (ESI) available. See DOI: 10.1039/c9cy00436j

interesting correlation between the size of the oxygen vacancy clusters and promotion of the reducibility and activity of the ceria nanorods in the CO oxidation reaction.

The oxidation of low concentration formaldehyde in air over Au/CeO₂ in HCHO oxidation is well reported.^{15,25–27} It turns out that oxygen vacancies play a critical role in the HCHO oxidation reaction. In this respect, Jing *et al.*²⁰ found that the oxidation of HCHO is more favorable on Au/Ce_{1–x}O_{2–y} than on Au/CeO₂, which is consistent with the co-adsorption of HCHO and O₂ on the defective CeO₂ surface. The presence of adsorbed active oxygen species contributed to the C–H cleavage and reduced the energetic cost of the HCHO oxidation reaction. Xu *et al.*²⁸ reported the importance of the shape and size control of ceria to give nanorods with {110} and {100} facets which present a relatively low energy for oxygen vacancy formation. Furthermore, Li *et al.*²⁹ reported on the beneficial role of the high surface area of ceria which provided a high density of oxygen vacancies and also reported the presence of high oxidation states of gold through the formation of a Au_xCe_{1–x}O_{2–δ} solid solution as potential centers for HCHO adsorption.

In order to gain more efficient catalysts for HCHO oxidation one possible strategy could be to dope ceria with another transition metal (TM) by researching the synergetic effect between the two TM oxides allowing better activation of the Au species and a better mobility of the active oxygen species on the catalyst surface.

In this way, the performances of Au–CeO₂–Co₃O₄ based catalysts were investigated in HCHO oxidation.^{30,31} Liu *et al.*³¹ reported 100% HCHO conversion into CO₂ at a temperature of about 39 °C over a three-dimensionally ordered macroporous (3DOM) Au/CeO₂–Co₃O₄ catalyst performed better than a 3DOM Au/CeO₂ catalyst. A synergetic effect between Co₃O₄ and CeO₂ through the participation of Co₃O₄ in the oxygen transfer during the HCHO catalytic oxidation process was proposed by the authors to account for this behavior.

In this paper we present a novel approach for the synthesis of Au/CeO₂–Co₃O₄ catalysts based on the dispersion of gold (1.5 and 3 wt%) by deposition–precipitation (DP) over Co-promoted ceria (Co: 9 and 12 mol%) and un-promoted ceria synthesized using the hydrothermal method. Both the catalytic reactivity and stability of the as-prepared samples towards HCHO oxidation were examined. The fresh catalysts were characterized extensively using X-ray diffraction (XRD), Raman spectroscopy, N₂-physisorption, H₂ temperature-programmed reduction (H₂-TPR), X-ray photoelectron spectroscopy (XPS) and time-of-flight secondary ion mass spectrometry (ToF-SIMS). High-resolution transmission electron microscopy (HRTEM) images were registered for two selected catalysts. The catalytic performances are discussed in terms of the effects of the oxygen vacancies.

Experimental details

Materials synthesis

Cerium based oxides were prepared *via* the hydrothermal method, adapted from the research published by Xu *et al.*²⁸

Typically, for pure ceria preparation, 6 g of Ce(NO₃)₃·6H₂O (Aldrich, 99%) was dissolved in 30 mL of H₂O and 40 mL of NaOH (2.5 mol L^{–1}; Aldrich, >98%) was added to the solution under vigorous stirring. The resulting suspension was rapidly transferred into a 100 mL Teflon autoclave and heated in an oven at 120 °C for 23 h. The aged precipitate was collected by filtration, washed with deionized water until neutral and finally with ethanol. The resulting powder was dried overnight at 60 °C and calcined at 350 °C for 3 h (heating rate 2 °C min^{–1}). This sample was denoted as Ce.

For the Co-promoted ceria preparation, the same experimental procedure was used except that an appropriate amount of Co(NO₃)₂·6H₂O (Aldrich, 99%) was simultaneously added with the cerium(III) nitrate into 30 mL of H₂O. These samples were denoted as CeCox with *x* = 9 or 12, expressing the Co molar percentage.

For the synthesis of the Au based catalysts, an appropriate volume of HAuCl₄·3H₂O (0.01 mol L^{–1}; Aldrich, 99.999%) was added to an aqueous suspension of the ceria based support and stirred for 1 h. At that stage, the pH of the solution was fixed at approximately 7.5–8.0 by adding K₂CO₃ (0.05 mol L^{–1}; Aldrich > 99%) and the temperature was allowed to increase to 65 °C. The suspension was stirred overnight. After filtering and careful washing with hot (50 °C) deionized water, the powder was dried overnight at 80 °C before being calcined at 350 °C for 2 h (heating rate 2 °C min^{–1}). These samples were denoted as *y*Au/CeCox with *y* = 1.5 or 3, expressing the Au weight percentage.

Material characterization

N₂ adsorption–desorption isotherms were measured at the temperature of liquid nitrogen, using a gas adsorption analyzer (TriStar II 3020). The sample was heated at 100 °C for 3 h under vacuum before measurement. The pore volume was determined at *P*/*P*₀ = 0.99. The Brunauer–Emmett–Teller (BET) method was used to calculate the specific surface areas. The Barrett–Joyner–Halenda (BJH) model was used to estimate the pore size distributions.

X-ray diffraction measurements were carried out using a Bruker D5000 vertical goniometer equipped with a Cu anode (Kα radiation λ = 1.5418 Å) and a graphite monochromator. A proportional counter and a 0.05° step size in 2θ were used. The integration time was 10 s per step and the scan range was from 20 to 80° in 2θ. The assignment of the various crystalline phases was based on comparison with files in the ICSD (Inorganic Crystal structure data base). The mean crystallite size (*d*) of the CeO₂ phase was calculated from the line broadening of the most intense reflection (111) using the Scherrer equation.

High-resolution transmission electron microscopy characterization was performed using a TECNAI TEM operating at an accelerating voltage of 200 kV. The prepared powders were deposited onto a carbon-coated copper grid for TEM observation.

The Raman spectra were recorded with a XY800 Raman Dilor spectrometer equipped with an optical multichannel detector (liquid nitrogen-cooled charge coupled device). The 647.1 nm excitation line of a Spectra Physics ion laser with very low power (3 mW) was focused on the compounds using the macroscopic configuration. LABSPEC software allowed us to realize acquisitions and perform data processing. Micro-Raman spectroscopy measurements were also performed with a Horiba Jobin-Yvon Labram infinity instrument, equipped with a liquid nitrogen cooled CCD detector. The Raman spectra were recorded at $\lambda = 532$ nm with a laser power of 0.6 mW. Spectra were recorded in the *ex situ* mode at room temperature in ambient air. The $I_{\text{DEF}}/I_{\text{F}_{2g}}$ ratio was determined using the following procedure. The area of the F_{2g} component was first extracted from the area of the half-peak positioned on the low Raman shift. The DEF component was deduced from the difference between the total area of the envelope and that of the F_{2g} component.

Redox properties of the samples were evaluated using a conventional temperature-programmed reduction apparatus (Micromeritics model AutoChem II) which monitored the hydrogen consumption of the sample. 50 mg of the sample was placed in a quartz reactor and heated in flowing air (50 mL min^{-1}) at 150 °C for 0.5 h and then cooled down to 20 °C. Then, the reactor was heated from 20 to 1000 °C with a heating rate of 10 °C min^{-1} in a gas mixture (5 vol% H_2 + 95 vol% Ar, 50 mL min^{-1}).

The XPS analyses were performed using a VG Microtech ESCA 3000Multilab, equipped with a dual Mg/Al anode. The unmonochromatized Al $K\alpha$ radiation (1486.6 eV) was used as the excitation source. The sample powders were analyzed as pellets, mounted on double-sided adhesive tape. The pressure in the analysis chamber was in the range of 10^{-8} Torr during data collection. The binding energies (BE) of the different core levels were referred to the Ce u^{iii} component associated to the Ce $3d_{3/2}$ component set at 916.7 eV. Rapid scans of the Ce 3d region were performed before each analysis in order to evaluate the Ce^{3+} percentage avoiding possible Ce^{4+} reduction under the beam.³² Analyses of the peaks were performed using the software CasaXPS. Atomic concentrations were calculated from the peak intensity using the sensitivity factors provided in the software. The BE are quoted with a precision of ± 0.15 eV and the atomic percentage with a precision of $\pm 10\%$.

The ToF-SIMS data were acquired using a ToF-SIMS⁵ spectrometer (ION-TOF GmbH Germany) equipped with a bismuth liquid metal ion gun (LMIG). The samples were bombarded with a pulsed Bi_3^+ primary ion beam (25 keV, 0.25 pA) rastered over a 500×500 μm surface area. With a data acquisition of 100 s, the total fluence did not amount to 1012 ions/ cm^2 ensuring static conditions. Charge effects were compensated by means of a 20 eV pulsed electron flood gun. Data were collected over a mass range of $m/z = 0$ –1200 for both positive and negative secondary ions. The fragments were identified by their exact mass, coupled with the appropriate intensities for the expected isotope pattern.

Catalytic performances

The catalytic oxidation of formaldehyde was performed in a fixed-bed reactor (internal diameter = 10 mm) loaded with the catalyst. Before each test, the catalyst was pre-treated for 1 h at 300 °C under an O_2 (20 vol%)/ N_2 flow (100 mL min^{-1}) to remove water and surface impurities. Gaseous formaldehyde was generated from para-formaldehyde in a permeation tube placed in a permeation chamber (Dynacalibrator, VICI Metronics Inc.). By adjusting the gas carrier flow (O_2 (20 vol%)/ N_2) at 100 mL min^{-1} and the chamber temperature at 100 °C, a stable formaldehyde concentration of 100 ppmv was generated.

After pre-treatment, the reactive flow was flushed over the catalyst at 300 °C for 1 h and the temperature was then allowed to decrease from 300 to 40 °C (0.5 °C min^{-1} until 100 °C and 0.2 °C min^{-1} until 40 °C) when using free-Au catalysts. In the case of the Au based catalysts, the temperature was allowed to decrease from 300 to 100 °C in air. At that stage the reactive mixture was introduced into the reactor and after 1 h under that mixture, the temperature was allowed to decrease from 100 to 25 °C (0.2 °C min^{-1}). The catalysts were then treated for 1 h at 25 °C in dry air under the same operating parameters ([HCHO]: 100 ppmv, total flow rate: 100 mL min^{-1}). Following this the test of durability was performed for 40 h at 25 °C.

The HCHO oxidation tests were performed over 200 mg (free-Au based catalysts) or 100 mg (Au based catalysts). The effluent gases were analyzed online with a Varian CP-4900 Micro-GC equipped with a thermal conductivity detector and COX type column (1 m). The formaldehyde conversion (X_{HCHO} , %) was evaluated using the following equation:

$$X_{\text{HCHO}}(\%) = 100 \times [\text{CO}_2]/[\text{HCHO}]_{\text{ini}}$$

In which $[\text{CO}_2]$ is the concentration of CO_2 at time t and $[\text{HCHO}]_{\text{ini}}$ is the initial concentration of formaldehyde.

Results and discussion

Textural properties

N_2 adsorption-desorption isotherms of the supports are shown in Fig. S1a†. The ceria based samples showed isotherms of type IV with a narrow hysteresis loop for the Co-promoted ceria ($P/P_0 = 0.85$ to 1 compared to $P/P_0 = 0.9$ to 1 with Co-free ceria). After Co addition, a decrease of about 25% of the SSA compared to pure ceria was observed (Table 1) accompanied by pore size distribution enlargement, while the pore volumes remained unchanged. These results may suggest that cobalt addition affects the morphology of ceria. It is generally reported in the literature that when TM ions were promoted in the ceria structure, the specific surface area (SSA) increased because of the decrease in the crystallization of the metal promoted cerium based oxides.^{33,34} Based on our results, it can be proposed that small particles of the cobalt oxides are formed at the CeO_2 external surface, contributing to the SSA decrease. Au introduction on the supports did not significantly change the isotherms shape (Fig. S2a†). For the

Table 1 Textural and structural properties of Ce, CeCox and yAu/CeCox samples

Sample	$S_{\text{BET}}/\text{m}^2 \text{ g}^{-1}$	Pore volume/ $\text{cm}^3 \text{ g}^{-1}$	Average pore size/nm	$d(\text{CeO}_2)/\text{nm}$	$I_{\text{DEF}}/I_{\text{F}_{2g}}^a$
Ce	111	0.50	20	10	0.10
CeCo9	82	0.54	32	12	0.33
CeCo12	89	0.56	32	13	0.42
1.5Au/Ce	116	0.42	13	10	0.38
3Au/Ce	107	0.38	15	10	0.51
1.5Au/CeCo9	79	0.44	24	12	0.50
3Au/CeCo9	80	0.41	22	12	0.55
3Au/CeCo12	85	0.44	19	13	0.58

^a I_{DEF} corresponds to the intensity of the Raman lines owing to ceria defects; ($>470 \text{ cm}^{-1}$).

same support composition, the porous volume and average pore size were slightly decreased without significant variation in the SSA values (Table 1). This suggests that well dispersed gold nanoparticles are present at the support surface.

Structural properties

The XRD patterns of the different samples are shown in Fig. 1. The peaks at $2\theta = 28.5^\circ, 33.0^\circ, 47.4^\circ, 56.2^\circ, 59.0^\circ, 69.4^\circ, 76.6^\circ$ and 79.0° correspond to diffraction from the (111), (200), (220), (311), (222), (400), (331) and (420) planes of the fluorite CeO_2 structure, respectively (JCPDS PDF no. 34-0394). After doping with cobalt, the XRD patterns were quite similar to pure ceria. The CeO_2 diffraction peaks were not shifted and the average crystallite size of ceria was unchanged (Table 1). It is generally observed that when Co is

introduced into CeO_2 , a gradual ceria peak shift towards a higher angle side and decrease in the ceria crystallite size occur with a Co concentration increase.^{35–37} This is explained by the incorporation of smaller Co^{2+} and/or Co^{3+} cations into the Ce^{4+} ion sites,³⁸ leading to a decrease in the unit cell volume. However to accommodate the change in size, some authors propose that up to 5 at%, the incorporation of Co^{2+} causes the reduction of Ce^{4+} into Ce^{3+} leading to the reverse observation, that is an increase in the crystallite size and lattice parameter^{39,40} with a shift to the lower angles. The decrease in crystallite size is generally accompanied with an increase in the SSA.^{37,41} Conversely, a decrease in the SSA observed for the CeCo9 and CeCo12 samples supports the possible formation of a Co containing phase separate to the CeO_2 crystalline phase. In addition, a careful examination of the XRD patterns of the cobalt containing samples revealed small features attributed to the (311) planes of the Co_3O_4 spinel (JCPDS PDF no. 43-1003) which were observed in the 2θ range $35\text{--}40^\circ$ (Fig. S3†). After deposition of 1.5 wt% of gold, no diffraction peak for metallic Au (JCPDS PDF no. 66-0091) at $2\theta < 38.2^\circ$ (111) was detected, suggesting the presence of highly dispersed crystallites. In the case of Au 3 wt% a broad feature corresponding to the Au (111) peak can be noticed, this is probably due to the higher weight content and or a slight size increase with respect to the 1.5 wt% of gold (Fig. S3†). Owing to the low intensity and partial overlapping of the Au (111) and Co_3O_4 (222) peaks, it is not straightforward to evaluate the Au crystallite size.

In order to gain further insights into the Au particle size and shape, as well as the representative morphology of the CeO_2 and Co-promoted CeO_2 oxides, HR-TEM images were registered on two selected samples, 3Au/Ce and 3Au/CeCo9.

In Fig. 2 two representative images are shown.

Au nanoparticles around 5 nm were detected for 3Au/Ce (Fig. 2a), and slightly smaller (3–5 nm) gold particles were found in the case of 3Au/CeCo9 (Fig. 2b). Moreover, in accordance with the hydrothermal preparation method²⁸ used for the synthesis of the supports, the formation of CeO_2 nanorods (with a width around 5 nm and length in the range 30–100 nm) was very evident.

Raman spectroscopy was used to characterize the nature of the ceria support. For the sake of comparison with the Micro Raman spectrum of the as-made ceria, a commercial

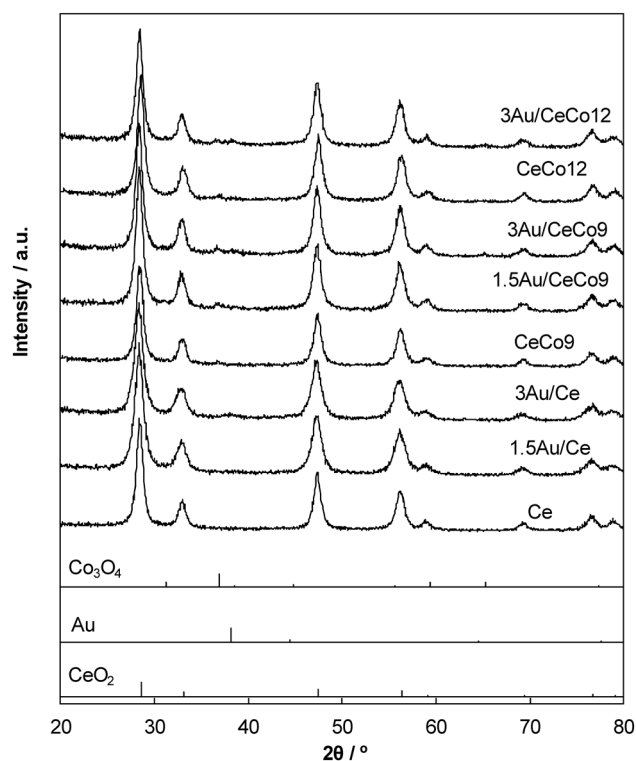


Fig. 1 XRD patterns for the Ce, CeCox and yAu/CeCox samples.

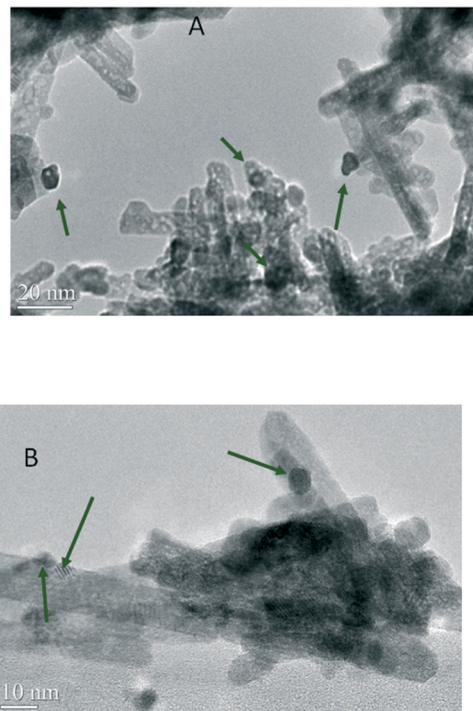


Fig. 2 HRTEM images of (A) 3Au/Ce and (B) 3Au/CeCo9.

CeO₂ (Aldrich) is also displayed in Fig. 3. The two Raman spectra were dominated by a strong peak assigned to the vibrational mode of F_{2g} symmetry in a cubic fluorite lattice. Interestingly, as compared to the Raman spectrum of the commercial CeO₂, the line shifts downwards (465 cm⁻¹ to 462 cm⁻¹), the line shape becomes broader (full-width half maximum (FWHM) × ≈ 3) and an asymmetric peak on the low-energy side appeared clearly. These three features attest of the nanocrystallinity of the Ce support compared to the commercial CeO₂ sample.⁴² Additionally, some broad and ill-defined peaks were found located at about 260, 420, 480 and

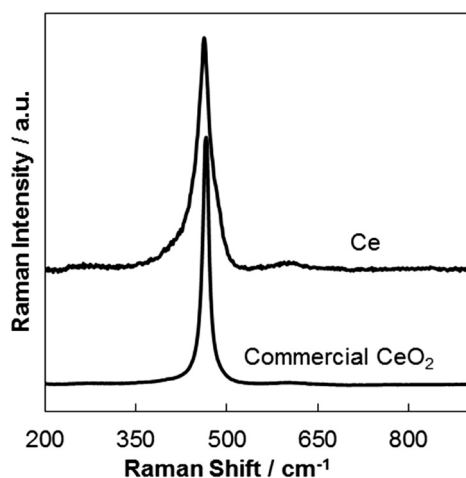


Fig. 3 Micro Raman spectra of the as-made ceria (Ce) and of a commercial CeO₂.

600 cm⁻¹ in accordance with the literature.⁴³ The lines in the 480–600 cm⁻¹ wavenumber range have been previously correlated to the presence of oxygen vacancies in ceria which are accompanied by the formation of reduced Ce³⁺ sites.^{44–46} The presence of lines in this energy range for Ce as compared to the commercial ceria indicates that smaller ceria particles possess an increased intrinsic capability towards oxygen vacancy formation. Recently an explanation for the origin of these experimentally observed lines within the 480–600 cm⁻¹ region has been reported based on the calculated Raman spectra of the reduced bulk ceria obtained from an *ab initio* density functional theory (DFT) study of the vibrational properties of ceria.⁴⁷ The reduced model systems display signature vibrational lines in the 480–600 cm⁻¹ region associated with the presence of oxygen defects and reduced Ce³⁺ ions. This study highlighted that the spectral properties were strongly influenced by the coordination cubes around Ce^{4+/3+} ions in CeO_{2-x}.⁴⁷ A clear distinction was made between the Raman lines arising from Ce³⁺ in direct proximity to the oxygen defect and those originating from the Ce³⁺ located in the second coordination sphere of the oxygen vacancy calculated at 500 and 480 cm⁻¹, respectively. Moreover, the 550 cm⁻¹ region was also assigned to the Ce³⁺O₇V₀^{••} coordination (*i.e.*, Ce³⁺ reduction close to a defect), whereas the 525 cm⁻¹ region was attributed to the Ce⁴⁺O₇V₀^{••} coordination cube. However, in the 550 cm⁻¹ region, as well as at higher wavenumbers, additional peaks with low intensity were predicted for all of the coordination cubes around the Ce^{4+/3+} ions, which cannot be explained on the basis of the simple coordination model presented above.

Fig. 4 exhibits the macro-Raman spectra of the Ce, CeCo_x and γAu/CeCo_x samples. To assess the influence of the added Co ions on the structure of cerium oxide the Raman spectra of Ce and CeCo₉ are directly compared in Fig. S4.† We observed an increase of the shoulder at 490 cm⁻¹ for the Co-containing ceria which can be related to a mode of vibration associated with a Ce³⁺O₈ cube. This observation can be attributed to an increase in the oxygen vacancy density induced by the partial incorporation of Co³⁺ in the ceria lattice. However, the Raman spectra of all Co promoted CeO_{2-x} exhibited an active Raman line at 693 cm⁻¹ which can be assigned to the presence of Co₃O₄. This is consistent with the micro Raman spectrum given in Fig. S5.† Thus, for some investigated grains, the characteristic Raman signature of Co₃O₄ can be clearly observed. The Raman spectrum exhibited five active Raman lines at 194, 480, 523, 618, and 693 cm⁻¹ in accordance with the literature.⁴⁸ The intensity ratio $I_{\text{DEF}}/I_{\text{F}_{2g}}$ has been estimated, I_{DEF} being the contribution of the Raman lines to the ceria defect lines >470 cm⁻¹ (Table 1). A direct comparison of the $I_{\text{DEF}}/I_{\text{F}_{2g}}$ ratios shows that the density of Ce³⁺O₈ polyhedrons increases with the Co content. Furthermore, for a given Co content, a gold promotion effect is also found for the defective entities. The Raman spectra for the γAu/CeCo_x samples indicated further defective ceria consistent with the relative increase of the intensity of the lines

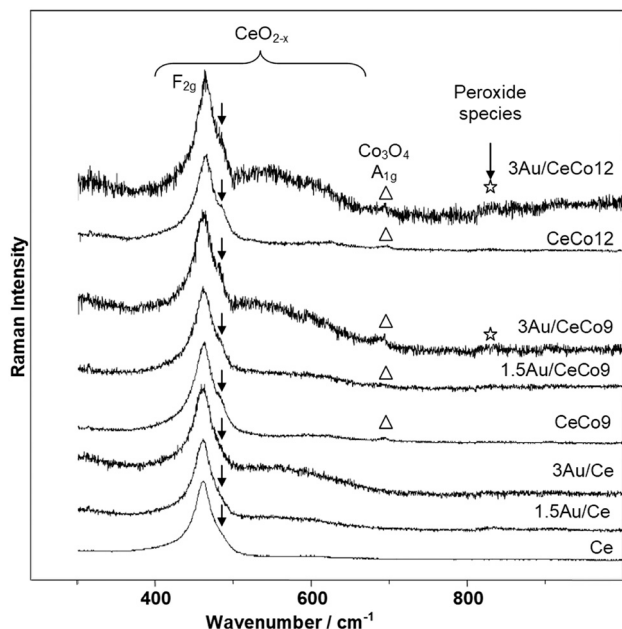


Fig. 4 Raman spectra of Ce, CeCox and yAu/CeCox samples.

localized in the defect band regions $480\text{--}600\text{ cm}^{-1}$. This indicates that gold promotes the density of $\text{Ce}^{3+}\text{O}_7\text{V}_0^{\bullet}$ and $\text{Ce}^{4+}\text{O}_7\text{V}_0^{\bullet}$ polyhedrons and even more when the gold content increases (Table 1).⁴⁷ It is worth noting that there was a line at 831 cm^{-1} which could be attributed to the nonplanar bridging peroxide species.⁴⁹ This result indicates that nanocrystalline CeO_2 stabilizes O_2 in part as a peroxide species.

Redox properties

The H_2 -TPR profiles of the supports are depicted in Fig. S6† and hydrogen consumption values are listed in Table 2. The pure ceria sample exhibited two main reduction regions denoted as medium temperature (MT) ($200 < T < 600\text{ }^\circ\text{C}$) and high temperature ($T > 600\text{ }^\circ\text{C}$). The H_2 consumption centered at around $450\text{ }^\circ\text{C}$ corresponds to the Ce^{4+} reduction from the uppermost layers, while the second one at a higher temperature (centered at around $900\text{ }^\circ\text{C}$) originates from the

reduction of the bulk CeO_2 .⁵⁰ The addition of cobalt to ceria modified the H_2 -TPR profiles. The reduction peak of the bulk ceria shifted to a lower temperature ($\sim 800\text{ }^\circ\text{C}$). The low temperature envelope between 200 and $400\text{ }^\circ\text{C}$ is similar to that obtained for the reduction of Co_3O_4 . The small peak at around $250\text{ }^\circ\text{C}$ can be assigned to the reduction of Co^{3+} to Co^{2+} , while the second one (around $300\text{ }^\circ\text{C}$) originates from Co^{2+} reduction to Co^0 .^{51,52} The shoulders of the peak at high temperature ($320\text{--}400\text{ }^\circ\text{C}$) could be assigned to the reduction of the surface CeO_2 . Therefore, in the presence of cobalt, the ceria (surface and bulk) reduction takes place at a much lower temperature. This could be explained by a hydrogen spillover effect on the metallic cobalt particles, which facilitates the ceria reduction.²⁶ A decrease in the hydrogen consumption for CeCo12 in comparison with CeCo9 was found (Table 2) consistent with the increase in the Ce^{3+} density in agreement with the Raman results. It is worth noting that the H_2 -TPR profiles obtained for the CeCo9 and CeCo12 samples are similar to those obtained for the $\text{Co}_3\text{O}_4\text{--CeO}_2$ catalysts prepared by impregnation of the Co species over a ceria support,^{53,54} confirming that the cobalt is mostly in the Co_3O_4 phase.

The H_2 -TPR profiles for the yAu/CeCox catalysts are depicted in Fig. 5. For all of the samples an additional low temperature (LT) ($T < 200\text{ }^\circ\text{C}$) H_2 consumption at $\sim 85\text{ }^\circ\text{C}$ was observed. This contribution comes from the surface ceria reduction, which can be largely facilitated by the presence of metallic Au sites at the interface with ceria through a hydrogen spillover effect.⁵⁰ The hydrogen consumption was similar for pure ceria and 1.5Au/Ce (Table 2). If we take into account the increase of the amount of Ce^{3+} through gold loading (Raman results), the expected H_2 consumption should be less than that of $0.81\text{ mmol H}_2\text{ g}^{-1}$ which is registered for ceria alone. The observed value for 1.5Au/Ce can be explained by the presence of some additional reducible cationic gold species into the catalyst. For 3Au/Ce, the further decrease in H_2 consumption can be related to the more defective ceria structure, as previously shown in the Raman spectroscopy results

Table 2 H_2 consumption values obtained for the Ce, CeCox and yAu/CeCox samples

Sample	LT ^a peak/ $\text{mmol H}_2\text{ g}^{-1}$	MT ^b peak/ $\text{mmol H}_2\text{ g}^{-1}$
Ce	—	0.81
CeCo9	—	1.48
CeCo12	—	1.37
1.5Au/Ce	0.81	—
3Au/Ce	0.59	—
1.5Au/CeCo9	0.47	0.74
3Au/CeCo9	0.42	0.71
3Au/CeCo12	0.41	0.62

^a Low temperature. ^b Medium temperature.

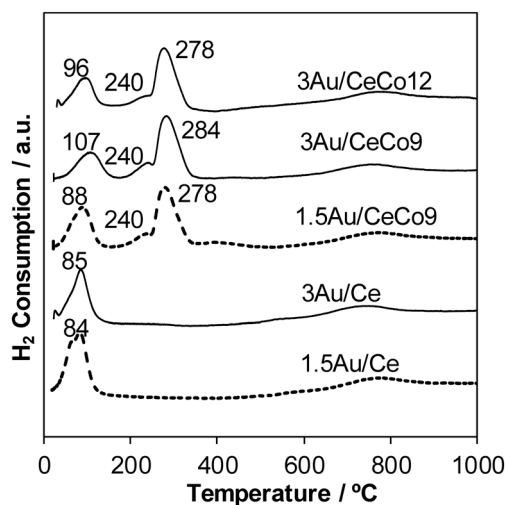


Fig. 5 H_2 -TPR profiles of fresh yAu/CeCox samples.

(Table 1). For the Au/CeCo_x catalysts, the low temperature (LT) H₂ consumption values decreased in comparison with those of the Au/Ce samples for an Au loading of 1.5 wt% loading (Table 2) confirming the beneficial role of cobalt in the formation of oxygen vacancies directly connected to the amount of Ce³⁺. Fig. 6 shows the possible correlation between low temperature H₂ consumption and the $I_{\text{DEF}}/I_{\text{F}_{2g}}$ Raman ratio for the γ Au/CeCo_x samples. The low temperature H₂ consumption values linearly decrease with the $I_{\text{DEF}}/I_{\text{F}_{2g}}$ Raman ratio, confirming that the density increase of the Ce³⁺O₇V_o^{••} entities is responsible for the lower H₂ consumption at a low temperature. In contrast to Au/CeO₂, the Co₃O₄ reduction observed between 200 and 350 °C (MT peak) seems to not be affected by the presence of metallic Au in terms of the peak position. The non-observance of the H₂ spillover effect can be explained by the absence of a close interaction between the Au sites and the Co₃O₄. This assumption can be related to the Co₃O₄ morphology effect in the gold assisted Co₃O₄ reduction.⁵⁵

Surface chemical properties

The detailed XPS results obtained for the different samples are summarized in Table 3. The Ce 3d signal has a complex satellite structure owing to the hybridization between the Ce 4f and O 2p states. To estimate the surface ratios of Ce³⁺ to the total amount of Ce species, the Ce 3d region was fitted according to the research published Burroughs *et al.*,⁵⁶ with ten components that take into account the spin orbit splitting Ce 3d_{5/2}–Ce 3d_{3/2} and other splitting caused by a redistribution of the entire energy spectrum after a core hole is created (Fig. S7†). There are four peaks (labelled as v⁰, u⁰, vⁱ, and uⁱ) attributed to Ce³⁺ and six peaks (labelled as v, u, vⁱⁱ, uⁱⁱ, vⁱⁱⁱ, and uⁱⁱⁱ) attributed to Ce⁴⁺. The data were fitted using the constraints existing between the corresponding compo-

Table 3 Summarized XPS results from the Ce 3d and Au 4f core-level spectra

Sample	Ce ³⁺ (%)	Ce ⁴⁺ (%)	Au 4f _{7/2} /eV	Au/Ce
Ce	16	84	—	—
1.5Au/Ce	21	79	85.3	0.05 (0.013)
3Au/Ce	19	81	85.3	0.09 (0.027)
CeCo9	15	85	—	—
1.5Au/CeCo9	15	85	85.0	0.05 (0.013)
3Au/CeCo9	18	82	84.9	0.09 (0.027)
CeCo12	15	85	—	—
3Au/CeCo12	17	83	84.8	0.10 (0.027)

The Au/Ce values in brackets correspond to the bulk ones.

nents 3d_{5/2}–3d_{3/2} given by Preisler *et al.*⁵⁷ All of the supports showed an analogous surface concentration for the Ce³⁺ species which increased in the corresponding Au catalysts (Table 3).

The Au 4f region showed the two spin-orbit components Au 4f_{7/2} and Au 4f_{5/2} (Fig. 7). The Au 4f_{7/2} BE are listed in Table 3. The maximum of the Au 4f_{7/2} photopeak was located at 85.3 eV for the Au/Ce samples, and it was located at a lower binding energy (84.9 eV) for the Au/CeCo_x samples. These BE values correspond to the presence of the Au⁺ species, without excluding the possibility of metallic gold to some extent. The observed decrease of the BE in the presence of Co is indicative of the presence of less oxidized gold and can be explained by the reduced Au–CeO₂ interface.

The variations of the XPS Au/Ce atomic ratio are consistent with the increase of the gold content in the sample. The

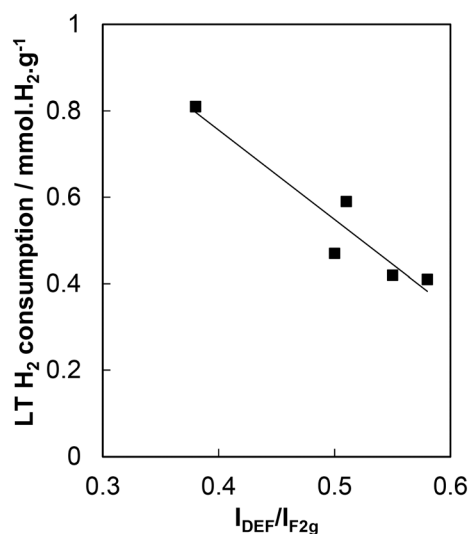


Fig. 6 LT H₂ consumption as a function of the $I_{\text{DEF}}/I_{\text{F}_{2g}}$ Raman ratio for γ Au/CeCo_x samples.

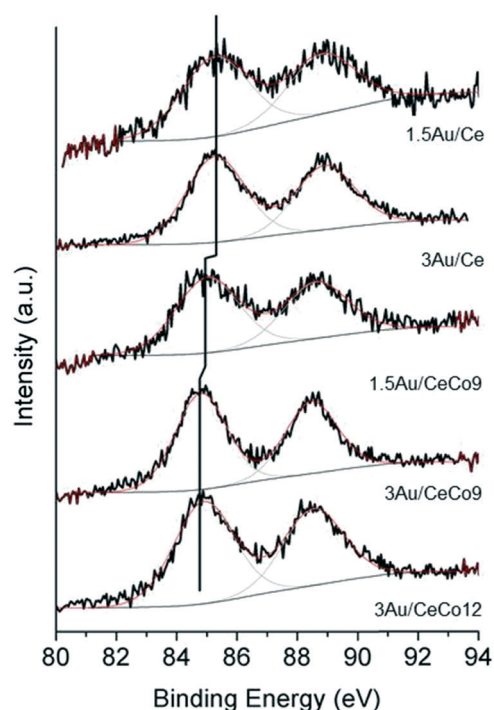


Fig. 7 XPS Au 4f signal obtained for γ Au/CeCo_x.

larger XPS experimental values with respect to the bulk ones (Table 3) suggest that gold species are located on top of the ceria nanoparticles. Moreover, the finding that the XPS Au/Ce atomic ratio measured for the catalysts with Au 1 wt% doubled for an Au loading of 3%, confirming the comparable Au particle size for all of the prepared catalysts.

Static ToF-SIMS were used to probe the 3–4 outermost layers of the samples. Indeed, static ToF-SIMS allow the salient atomic and molecular information of the surface structure to be obtained.⁵⁸

Fig. 8 shows the ToF-SIMS spectrum in the m/z (195–240) range obtained from the 1.5Au/CeCo9 sample. Along with the peak located at $m/z = 197$ assigned to Au^- , secondary ions located at $m/z = 213, 214, 229$ and 230 were found and assigned to AuO^- , AuOH^- , AuO_2^- and AuO_2H^- , respectively. The detection of such entities indicates the presence of some oxidized gold in line with previous work.⁵⁹ It is worth noting that a decrease in the $\text{AuO}_2^-/\text{Au}^-$ ratio by a factor of about 2 for both ceria and Co promoted ceria supported gold catalysts is consistent with a decrease in the rate of oxidized gold with Au loading.

In order to investigate the role of cobalt and gold on oxygen defective CeO_{2-x} , the evolution of the $\text{CeO}_2^+/\text{CeO}^+$ ratio was investigated as a function of the nature of the samples (Table 4). It was found that a slight decrease of that ratio was indicative of a more defective ceria surface, with Co or/and Au addition, and this decrease is all the more important as the Au(Co) content increases. Furthermore, ToF-SIMS studies revealed gold–ceria and cobalt–ceria interactions through the formation of secondary ions such as CeAuO_2H^- and CoCeO_2^+ , $\text{Ce}_2\text{CoO}_4^+$, $\text{Ce}_3\text{CoO}_5^+$ and $\text{Ce}_4\text{CoO}_7^+$, respectively. It is worth noting that $\text{Au}_x\text{O}_y\text{Co}_z^{\pm}$ ions were not detected ruling out some possible interactions between Au and Co. This result is consistent with the H_2 -TPR results, suggesting the absence of an interaction between Au and Co. Interestingly, the presence of the secondary ion Co_3O_4^- ($m/z = 240$) in connection with the presence of the cobalt spinel oxide on both Co containing samples was found, which is in agreement with the XRD and Raman results. It should be noted that the $\text{CeAuO}_2^-/\text{Au}^-$ intensity ratio significantly decreased with the Au content as shown in Fig. S8,† suggesting a decrease of the gold–ceria

interface related to the relative decrease of the oxidized gold content.

The presence of chloride ions Cl^- was also observed to be linked to the nature of the gold precursor, which is HAuCl_4 . Such observation using ToF-SIMS⁶⁰ is important knowing that chloride may have a great impact on the catalytic performance. The intensity ratio of Cl^-/total allowed information to be obtained about the extent of chlorine contamination (Table S1†). This ratio increased in the presence of gold content. The intensity ratio was about one order of magnitude higher for 1.5AuCe than for 3AuCe and rather similar features were observed for the Co–Au samples. As the magnitude, but also the location of Cl^- is of importance, possible direct interactions between Cl^- and Ce, Co and Au have been investigated. It is worth mentioning that the CoCl^\pm secondary ions, in contrast to AuCl^- , were not observed. This clearly indicates the presence of chloride ions in the surrounding gold centers. A decrease of the $\text{AuCl}_2^-/\text{Au}^-$ intensity ratios from 1.5AuCe(Co) to 3.0AuCe(Co) indicates that the amount of gold bonded to Cl^- increases with the decreasing Au content. This is not accompanied by the agglomeration of gold as the $\text{Au}_4^-/\text{Au}^-$ intensity ratios remained lower for the 1.5 Au wt% samples. No $\text{Au}_x\text{Cl}_y\text{O}_z^\pm$ ions were detected, suggesting that the presence of Cl^- induces the formation of the AuCl_3 entities, in line with the observation of the AuCl^- , AuCl_2^- and AuCl_3^- ions (in m/z) at 232, 267 and 302, respectively. The reverse correlation can be made when considering the $\text{CeCl}_2^+/\text{Ce}^+$ intensity ratios. Regarding Co, the formation of the oxichlorocobalt species is expected to be consistent with the detection of CoOCl ions.

Catalytic properties

The HCHO light-off curves for the prepared supports are shown in Fig. S9.† The pure ceria support was poorly active, reaching 40% HCHO conversion in CO_2 at 300 °C. However, doping CeO_2 with Co significantly enhanced the catalytic activity and whatever the cobalt content the total conversion of formaldehyde was obtained at 250 °C. The higher activity for HCHO oxidation of the CoCe oxides in comparison with that of pure CeO_2 can be explained by the higher redox properties of the composite owing to the combination of the redox properties of both oxides, that is the reduction of Co_3O_4 and the assisted reduction of CeO_2 in the vicinity of the cobalt species, as suggested by the H_2 -TPR analysis. Indeed, when studying pure Co_3O_4 , Fan *et al.*⁶¹ proposed that Co^{3+} ions act as active sites for total formaldehyde oxidation. Dioxygen can be activated over ceria oxygen vacancies.⁶² Therefore, it can be proposed that Co^{3+} could be reduced by HCHO into Co^{2+} , while activated oxygen transforms Ce^{3+} into Ce^{4+} . A continuous oxygen transfer from CeO_2 to CoO could occur through the synergistic effect between CeO_2 and Co_3O_4 as illustrated in Scheme S1.† The HCHO light-off curves for the Au/Ce and Au/CeCo catalysts are shown in Fig. 9A. A remarkable improvement in the HCHO oxidation activity was observed when Au is added to the supports, with full conversion being achieved at around 100 °C for all of the catalysts. For the Au/

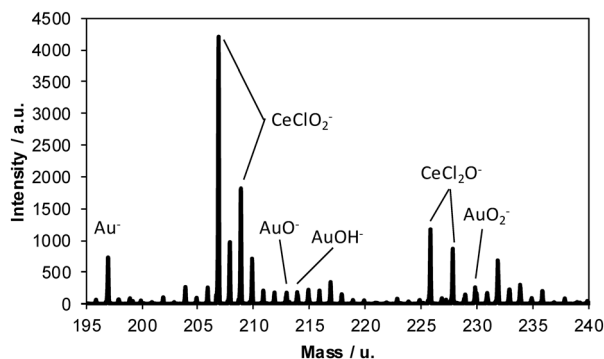


Fig. 8 Negative m/z (195–240) ToF-SIMS spectrum for the 1.5Au/CeCo9 sample.

Table 4 $\text{AuO}_2^-/\text{Au}^-$ and $\text{CeO}_2^+/\text{CeO}^+$ ratios extracted from the ToF-SIMS spectra

Sample	Ce	CeCo9	CeCo12	1.5Au/Ce	3Au/Ce	1.5Au/CeCo9	3Au/CeCo12
$\text{AuO}_2^-/\text{Au}^-$	—	—	—	0.38	0.16	0.26	0.12
$\text{CeO}_2^+/\text{CeO}^+$	0.014	0.014	0.011	0.013	0.011	0.015	0.011

CeO_2 samples, the two-fold gold content increase allowed the HCHO conversion into CO_2 to rise from 20% to 90% at 25 °C, respectively. Starting from 60 °C, the difference in conversion was much less pronounced owing to the significant increase of HCHO oxidation in the temperature range of 20–60 °C in the presence of the Au1.5/Ce catalyst (Fig. 9A). The effect of gold loading on formaldehyde oxidation has already been addressed by several authors. Regardless of the support used, for example, ZrO_2 ,¹⁴ FeOx ,¹³ CeO_2 ,²⁷ it is generally highlighted that increasing the gold content results in en-

hancement of the catalytic performance in formaldehyde oxidation. The addition of slight amounts of Co (9 or 12 mol%) notably boosted the formaldehyde conversion of the Au/CeO₂ materials. The results were especially impressive with a lower gold content (1.5 wt%) as 80% of HCHO conversion at 25 °C was obtained for 1.5Au/CeCo9, while the unmodified 1.5Au/Ce catalyst achieved the same conversion at around 60 °C. Lakshmanan *et al.*⁶² demonstrated that gold nanoparticles enhanced the oxygen storage capacity and the rate of oxygen exchange and promoted the activation of dioxygen by generating O_2^{2-} species at the gold/ceria interface perimeter. This result is consistent with the observance of a peroxo species (O_2^{2-}) using Raman spectroscopy for the 3Au/CeCo_x samples.

The durability tests over Au related catalysts are shown in Fig. 9b. An increase was observed for the HCHO conversion in the first hours of the test, except for the 1.5Au/Ce catalyst, for which the conversion always increased with time but at a lower rate. This induction period can be related to the reactive desorption of the chemically intermediate species resulting from the partial oxidation of HCHO, such as formates. After the induction period, the HCHO conversion into CO_2 with time remained rather stable or decreased to a lesser extent with time.

The HCHO conversion obtained at $t = 0$ h increased with the Raman ratio $I_{\text{DEF}}/I_{\text{F}_{2g}}$ (Table 1). This clearly shows the beneficial role of oxygen vacancies in HCHO total oxidation. The positive role of cobalt in the formation of oxygen vacancies could be the cause of the better activity. The increase of defects in the ceria was highlighted by the increase of $\text{Ce}^{3+}\text{O}_7\text{V}_\text{o}^-$ entities (Raman analysis) and by the increasing amount of Ce^{3+} species in line with the reduced amounts of H_2 consumption observed on H_2 -TPR upon adding Co. It is well known that oxygen vacancies allow greater oxygen mobility and the formation of oxygen active species that can improve the oxidation of the reaction intermediates. The correlation between the HCHO conversion into CO_2 and the $I_{\text{DEF}}/I_{\text{F}_{2g}}$ Raman ratio clearly supports the fact that the amount of oxygen vacancies play a critical role in the HCHO total oxidation.

The catalytic activity was compared in terms of the activity expressed as μmole of HCHO converted into CO_2 per second and per gram of Au, after 40 h of testing. The data are compared to those obtained at $t = 0$ h and are also listed in Table 5.

As reported in Table 5, all catalysts exhibited similar activities of about $2 \mu\text{mol s}^{-1} \text{g}_{\text{Au}}^{-1}$ except for 1.5Au/CeCo9 which displayed a two-fold activity, namely $3.9 \mu\text{mol s}^{-1} \text{g}_{\text{Au}}^{-1}$ at 40 h. The absence of a gold dispersion modification revealed by the XPS data between the 1.5Au/Ce and 1.5Au/CeCo9 samples cannot explain this improvement in the activity. In contrast,

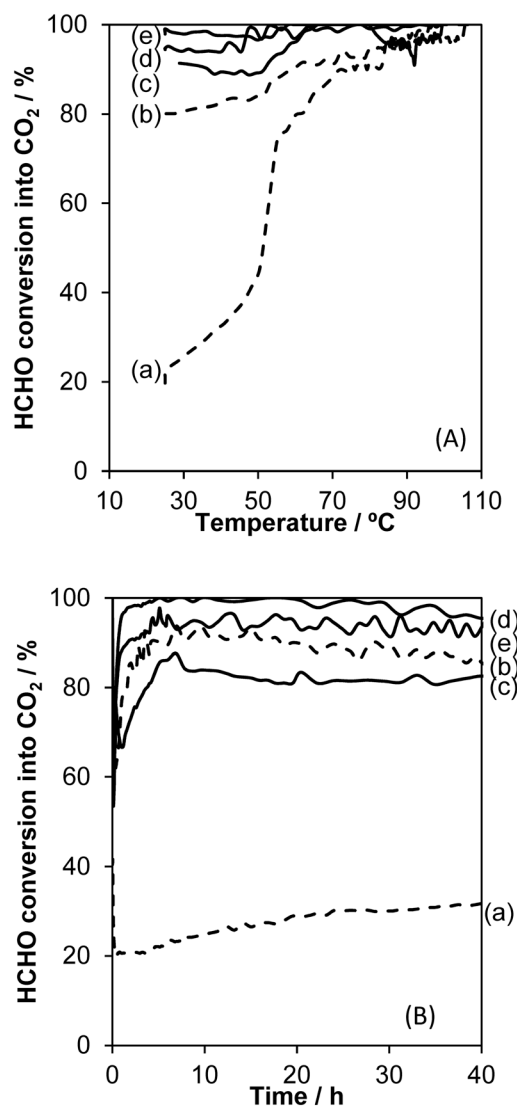


Fig. 9 HCHO conversion into CO_2 for the: (a) 1.5Au/Ce; (b) 1.5Au/CeCo9; (c) 3Au/Ce; (d) 3Au/CeCo12 and (e) 3Au/CeCo9 catalysts. (A) As a function of the decreasing temperature; and (B) at 25 °C for 40 h.

Table 5 Catalytic results for HCHO oxidized at 25 °C

Catalysts	Activity ^a /μmol s ⁻¹ g _{Au} ⁻¹	
	<i>t</i> = 0	<i>t</i> = 40 h
1.5Au/Ce	0.9	1.5
3Au/Ce	1.6	1.9
1.5Au/CeCo9	2.9	3.9
3Au/CeCo9	1.2	2.2
3Au/CeCo12	1.5	2.2

^a Activity measured at 25 °C.

an increase in the gold ceria interface, promoting oxygen vacancies, resulting in more oxidized gold species are recognized to be key parameters for increasing the activity over the 1.5Au/CeCo9 sample.

Conclusions

The effect of Co incorporation into Au/CeO₂-based catalysts has been investigated by varying the Co and Au content. The catalytic performances in HCHO oxidation were discussed in line with the physico-chemical characterizations of the fresh catalysts. BET, XRD, Raman and TPR characterization were performed on the Au/Co-promoted ceria catalysts and suggested that cobalt is mostly in the Co₃O₄ phase, no direct evidence of Co ions insertion into the CeO₂ lattice were found using XRD. The HRTEM images indicated the presence of Au particles around 5 nm and the formation of CeO₂ nanorods. The high dispersion of Au particles on the ceria top and a comparable Au size for all of the prepared catalysts were confirmed using XPS analysis.

The beneficial role of cobalt in the formation of oxygen vacancies directly connected to the Ce³⁺ amount was proven using Raman and TPR. The oxygen vacancies formed play a double role in enhancing the HCHO catalytic activity of the Au/Co-promoted CeO₂ catalysts: Ce³⁺ ions represent nucleation centers for the stabilization of the active Au ionic species and, at the same time, gaseous oxygen is easily activated over these centers. The presence of close gold–ceria and cobalt–ceria interactions were further confirmed using ToF-SIMS studies, and no Au_xO_yCo_z[±] ions were detected, ruling out some of the possible Au–Co contact.

Conflicts of interest

There are no conflicts to declare.

Acknowledgements

Leonarda Francesca Liotta thanks the University of Lille for the visiting professor position. This research is carried out in the field of the COST Action 17136 (Indoor Air Pollution Network), has been partially supported by a French–Italian project (PHC Galilée N°39624UG) and by an European Program INTERREG V France–Wallonie–Flanders (FEDER) (DepollutAir). Chevreul Institute (FR 2638), Ministère de l'Enseignement Supérieur et de la Recherche and Région Hauts-de-France are

also acknowledged for supporting this work. The authors thank Jean-Charles Morin, Nicolas Nuns, Olivier Gardoll, Christine Lancelot and Laurence Burylo for their contribution to the Raman, ToF-SIMS, H₂-TPR, HRTEM and XRD measurements, respectively.

Notes and references

- 1 IARC, *IARC Monogr. Eval. Carcinog. Risks Hum.*, 1982, **29**, 345–389.
- 2 J. Q. Torres, S. Royer, J. P. Bellat, J. M. Giraudon and J. F. Lamoniér, *ChemSusChem*, 2013(6), 578–592.
- 3 G. Zhang, Y. Hong and W. He, *Indoor Built Environ.*, 2015, **24**, 138–144.
- 4 L. Qi, B. Cheng, J. Yu and W. Ho, *J. Hazard. Mater.*, 2016, **301**, 522–530.
- 5 H. Tan, J. Wang, S. Yu and K. Zhou, *Environ. Sci. Technol.*, 2015, **49**, 8675–8682.
- 6 G. Pang, D. Wang, Y. Zhang, C. Ma and Z. Hao, *Front. Environ. Sci. Eng.*, 2016, **10**, 447–457.
- 7 M. Haruta, *J. Catal.*, 1989, **115**, 301–309.
- 8 B. Chen, X. Zhu, Y. Wang, L. Yu and C. Shi, *Chin. J. Catal.*, 2016, **37**, 1729–1737.
- 9 S. Scire and L. F. Liotta, *Appl. Catal., B*, 2012, **125**, 222–246.
- 10 Z. Tang, W. Zhang, Y. Li, Z. Huang, H. Guo, F. Wu and J. Li, *Appl. Surf. Sci.*, 2016, **364**, 75–80.
- 11 B.-B. Chen, X.-B. Zhu, Y.-D. Wang, L.-M. Yu, J.-Q. Lu and C. Shi, *Catal. Today*, 2017, **281**, 512–519.
- 12 B. B. Chen, C. Shi, M. Crocker, Y. Wang and A. M. Zhu, *Appl. Catal., B*, 2013, **132–133**, 245–255.
- 13 C. Li, Y. Shen, M. Jia, S. Sheng, M. O. Adebajo and H. Zhu, *Catal. Commun.*, 2008, **9**, 355–361.
- 14 Y. C. Hong, K. Q. Sun, K. H. Han, G. Liu and B. Q. Xu, *Catal. Today*, 2010, **158**, 415–422.
- 15 Y. Shen, X. Yang, Y. Wang, Y. Zhang, H. Zhu, L. Gao and M. Jia, *Appl. Catal., B*, 2008, **79**, 142–148.
- 16 Y. Wang, B. B. Chen, M. Crocker, Y. J. Zhang, X. B. Zhu and C. Shi, *Catal. Commun.*, 2015, **59**, 195–200.
- 17 C. Ma, G. Pang, G. He, Y. Li, C. He and Z. Hao, *J. Environ. Sci.*, 2016, **39**, 77–85.
- 18 B. B. Chen, X. B. Zhu, M. Crocker, Y. Wang and C. Shi, *Appl. Catal., B*, 2014, **154–155**, 73–81.
- 19 M. Jia, Y. Shen, C. Li, Z. Bao and S. Sheng, *Catal. Lett.*, 2005, **99**, 235–239.
- 20 M. Jing, W. Song, L. Chen, S. Ma, J. Deng, H. Zheng, Y. Li, J. Liu and Z. Zhao, *J. Phys. Chem. C*, 2018, **122**, 438–448.
- 21 C. T. Campbell and C. H. F. Peden, *Science*, 2005, **309**, 713–714.
- 22 R. Brezny, T. Egami, E. Mamontov, S. Tyagi and M. Koranne, *J. Phys. Chem. B*, 2002, **104**, 11110–11116.
- 23 T. X. T. Sayle, S. C. Parker and C. R. A. Catlow, *Surf. Sci.*, 1994, **316**, 329–336.
- 24 X. Liu, K. Zhou, L. Wang, B. Wang and Y. Li, *J. Am. Chem. Soc.*, 2009, **131**, 3140–3141.
- 25 B. Liu, C. Li, Y. Zhang, Y. Liu, W. Hu, Q. Wang, L. Han and J. Zhang, *Appl. Catal., B*, 2012, **111–112**, 467–475.

- 26 Y. Liu, B. Liu, Q. Wang, C. Li, W. Hu, Y. Liu, P. Jing, W. Zhao and J. Zhang, *J. Catal.*, 2012, **296**, 65–76.
- 27 J. Zhang, Y. Jin, C. Li, Y. Shen, L. Han, Z. Hu, X. Di and Z. Liu, *Appl. Catal., B*, 2009, **91**, 11–20.
- 28 Q. Xu, W. Lei, X. Li, X. Qi, J. Yu, G. Liu, J. Wang and P. Zhang, *Environ. Sci. Technol.*, 2014, **48**, 9702–9708.
- 29 H. F. Li, N. Zhang, P. Chen, M. F. Luo and J. Q. Lu, *Appl. Catal., B*, 2011, **110**, 279–285.
- 30 C. Ma, D. Wang, W. Xue, B. Dou, H. Wang and Z. Hao, *Environ. Sci. Technol.*, 2011, **45**, 3628–3634.
- 31 B. Liu, Y. Liu, C. Li, W. Hu, P. Jing, Q. Wang and J. Zhang, *Appl. Catal., B*, 2012, **127**, 47–58.
- 32 M. N. Revoy, R. W. J. Scott and A. P. Grosvenor, *J. Phys. Chem. C*, 2013, **117**, 10095–10105.
- 33 O. H. Laguna, F. R. Sarria, M. A. Centeno and J. A. Odriozola, *J. Catal.*, 2010, **276**, 360–370.
- 34 S. Yabe, M. Yamashita, S. Momose, K. Tahira, A. Yoshida, R. Li, S. Yin and T. Sato, *Int. J. Inorg. Mater.*, 2001, **3**, 1003–1008.
- 35 Y. A. S. Khadar, A. Balamurugan, V. P. Devarajan, R. Subramanian and S. D. Kumar, *Integr. Med. Res.*, 2018, 1–8.
- 36 S. Akram, Z. Wang, L. Chen, Q. Wang, G. Shen, N. Han, Y. Chen and G. Ge, *Catal. Commun.*, 2016, **73**, 123–127.
- 37 N. S. Arul, D. M. Pao and C. Chen, *J. Sol-Gel Sci. Technol.*, 2012, **64**, 515–523.
- 38 R. D. Shannon, *Acta Crystallogr., Sect. A: Cryst. Phys., Diffraction, Theor. Gen. Crystallogr.*, 1976, **32**, 751–767.
- 39 W. E. Mahmoud, A. A. Al-Ghamdi, F. A. Al-Agel, E. Al-Arfaj, F. S. Shokr, S. A. Al-Gahtany, A. Alshahrie, O. Jalled, L. M. Bronstein and G. W. Beall, *Mater. Res. Bull.*, 2015, **72**, 154–159.
- 40 R. Murugan, G. Vijayaprasath, T. Mahalingam and G. Ravi, *Ceram. Int.*, 2016, **42**, 11724–11731.
- 41 L. U. Suhong, W. Fan, C. Canchang, H. Fenglin and L. I. Kelun, *J. Rare Earths*, 2017, **35**, 867–874.
- 42 J. E. Spanier, R. D. Robinson, F. Zhang, S.-W. Chan and I. P. Herman, *Phys. Rev. B: Condens. Matter Mater. Phys.*, 2001, **64**, 245407.
- 43 J. Guzman, S. Carrettin and A. Corma, *J. Am. Chem. Soc.*, 2005, **127**, 3286–3287.
- 44 J. R. McBride, K. C. Hass, B. D. Poindexter and W. H. Weber, *J. Appl. Phys.*, 1994, **76**, 2435–2441.
- 45 T. Taniguchi, T. Watanabe, N. Sugiyama, A. K. Subramani, H. Wagata, N. Matsushita and M. Yoshimura, *J. Phys. Chem. C*, 2009, **113**, 19789–19793.
- 46 Z. Wu, M. Li, D. R. Mullins and S. H. Overbury, *ACS Catal.*, 2012, **2**, 2224–2234.
- 47 C. Schilling, A. Hofmann, C. Hess and M. V. Ganduglia-Pirovano, *J. Phys. Chem. C*, 2017, **121**, 20834–20849.
- 48 V. G. Hadjiev, M. N. Iliev and I. V. Vergilov, *J. Phys. C: Solid State Phys.*, 1988, **21**, L199–L201.
- 49 Y. Lee, G. He, A. J. Akey, R. Si, M. Flytzanistephanopoulos and I. P. Herman, *J. Am. Chem. Soc.*, 2011, **133**, 12952–12955.
- 50 Y. Liu, B. Liu, Y. Liu, Q. Wang, W. Hu, P. Jing, L. Liu, S. Yu and J. Zhang, *Appl. Catal., B*, 2013, **142–143**, 615–625.
- 51 S. S.-Y. Lin, D. H. Kim, M. H. Engelhard and S. Y. Ha, *J. Catal.*, 2010, **273**, 229–235.
- 52 P. Gawade, B. Bayram, A. M. C. Alexander and U. S. Ozkan, *Appl. Catal., B*, 2012, **128**, 21–30.
- 53 J. Y. Luo, M. Meng, X. Li, X. G. Li, Y. Q. Zha, T. D. Hu, Y. N. Xie and J. Zhang, *J. Catal.*, 2008, **254**, 310–324.
- 54 J. Dou, Y. Tang, L. Nie, C. M. Andolina, X. Zhang, S. House, Y. Li, J. Yang and F. Tao, *Catal. Today*, 2018, **311**, 48–55.
- 55 Y. Yao, L. L. Gu, W. Jiang, H. C. Sun, Q. Su, J. Zhao, W. J. Ji and C. T. Au, *Catal. Sci. Technol.*, 2016, **6**, 2349–2360.
- 56 P. Burroughs, A. Hamnett, A. F. Orchard and G. Thornton, *J. Chem. Soc. Dalt. Trans.*, 1976, **17**, 1686.
- 57 E. J. Preisler, O. J. Marsh, R. A. Beach and T. C. McGill, *J. Vac. Sci. Technol., B: Microelectron. Nanometer Struct.-Process., Meas., Phenom.*, 2001, **19**, 1611.
- 58 L. T. Weng, *Appl. Catal., A*, 2014, **474**, 203–210.
- 59 L. Fu, N. Q. Wu, J. H. Yang, F. Qu, D. L. Johnson, M. C. Kung, H. H. Kung and V. P. Dravid, *J. Phys. Chem. B*, 2005, **109**, 3704–3706.
- 60 I. Dobrosz-Gómez, I. Kocemba and J. M. Rynkowski, *Appl. Catal., B*, 2009, **88**, 83–97.
- 61 Z. Fan, W. Fang, Z. Zhang, M. Chen and W. Shangguan, *Catal. Commun.*, 2018, **103**, 10–14.
- 62 P. Lakshmanan, F. Averseng, N. Bion, L. Delannoy, J. M. Tatibouët and C. Louis, *Gold Bull.*, 2013, **46**, 233–242.